Dusty Outflows in Planetary Atmospheres: Understanding "Super-puffs" and Transmission Spectra of Sub-Neptunes

Lile Wang[1,2] and Fei Dai[2,3]

[1] Center for Computational Astrophysics, Flatiron Institute, New York, NY 10010, USA; lwang@flatironinstitute.org
[2] Princeton University Observatory, Princeton, NJ 08544, USA
[3] Department of Physics and Kavli Institute for Astrophysics and Space Research, Massachusetts Institute of Technology, Cambridge, MA 02139, USA

Abstract

"Super-puffs" are planets with anomalously low mean densities ($\lesssim 10^{-1}\,\mathrm{g\,cm^{-3}}$). With a low surface gravity, the extended atmosphere is susceptible to extreme hydrodynamic mass loss ("boil-off") on a timescale that is much shorter than the system's age. Even more puzzling, super-puffs are estimated to have a scale height of ~ 3000 km, yet recent observations revealed completely flat transmission spectra for Kepler 51b and 51d. We investigate a new scenario that explains both observations: non-static outflowing ($\dot{M} \gtrsim 10^{-10}\,M_\oplus\,\mathrm{yr^{-1}}$) atmospheres that carry very small dust grains ($\sim 10\,\text{Å}$ in size, $\sim 10^{-2}$ in mass fraction) to high altitudes ($\lesssim 10^{-6}$ bar). Dust at high altitudes inflates the observed transit radius of the planet while flattening the transmission spectra. Previous static atmospheric models struggle to achieve cloud elevation and production of photochemical haze at such high altitudes. We propose to test this scenario by extending the wavelength coverage of transmission spectra. If true, dusty atmospheric outflows may affect many young ($\lesssim 10^9$ yr), low-mass ($\lesssim 10\,M_\oplus$) exoplanets, thereby limiting our ability to study the atmospheric composition in transmission, and inflate the observed transit radius of a planet, hence obscuring the underlying mass–radius relationship.

Key words: methods: numerical – planets and satellites: atmospheres – planets and satellites: composition – planets and satellites: formation – planets and satellites: physical evolution

1. Introduction

"Super-puffs" are planets that have sub-Neptune masses ($\lesssim 5\,M_\oplus$) but gas-giant transit radii ($\gtrsim 5\,R_\oplus$), and thus extremely low mean densities ($< 10^{-1}\,\mathrm{g\,cm^{-3}}$) and large scale heights (~ 3000 km). A prime example is Kepler 51b, which has a $\sim 7 R_\oplus$ transit radius but a mass of only $\sim 2.1\,M_\oplus$ (consolidated by independent transit timing variation analyses of several groups, e.g., J. Roberts et al. 2019, in preparation; Masuda 2014, M14 hereafter). The ensemble of discovered super-puffs includes Kepler 51 c, 51d; Kepler 79d, 79e (Jontof-Hutter et al. 2014); and Kepler 87 c (Ofir et al. 2014). In this Letter we concentrate our discussions on the well-studied Kepler 51b unless specially noted.

Recent works (Owen & Wu 2017; Wang & Dai 2018, WD18 hereafter) suggest that hydrodynamic and photoevaporative loss of atmospheres might be a ubiquitous effect responsible of the observed bimodal radius distribution of close-in sub-Neptune planets (Fulton et al. 2017). Given their low surface gravity, super-puffs are expected to have excessive mass loss via photoevaporation (Lopez et al. 2012; Howe & Burrows 2015), or even without stellar high energy radiation ("boil-off", see also Owen & Wu 2016), and should disperse on a timescale of $\sim 10^3$ yr (Section 2.1), which is much shorter than the system's age (~ 0.3 Gyr for Kepler 51 from gyrochronology; M14). Similarly, Lammer et al. (2016) noted that CoRoT-24b must also have high-altitude aerosols to increase the apparent transit radius, thereby lowering the implied mass loss rate. However, they were agnostic of how aerosols could form or be lifted to such high altitudes.

Super-puffs, with their large scale heights, are considered ideal targets for transmission spectroscopy. However, the *Hubble Space Telescope* WFC3 observation of Kepler 51b and 51d has yielded flat transmission spectra in the near-infrared (Roberts et al. 2019, in preparation). This is reminiscent of the flat spectrum of GJ1214b (Kreidberg et al. 2014). If cloud/haze are invoked to mute the absorption features, they have to be advected to or produced at such a high altitude that current models would struggle (Section 2.2). We hereby consider a non-static atmosphere characterized by a slow hydrodynamic outflow ($\gtrsim 10^{-10}\,M_\oplus\,\mathrm{yr^{-1}}$), producing a relatively small mass loss over the age of Kepler 51. Dust grains can be carried to much higher altitude in this outflow, increasing the observed transit radius to $\sim 7\,R_\oplus$ while muting signatures of other species in the atmosphere.

2. Basic Ideas

2.1. Isothermal Atmosphere: Inevitable Escape

Generally a planetary atmosphere can be divided into a convective isentropic interior and a radiation-dominated, approximately isothermal exterior (Rafikov 2006; Ginzburg et al. 2016; Owen & Wu 2016). In the isothermal layer, hydrostatic density and pressure profiles are given by

$$p = p_\mathrm{p} \exp\left[\beta_\mathrm{p}\left(\frac{r_\mathrm{p}}{r} - 1\right)\right] \geqslant p_\infty = p_\mathrm{p} e^{-\beta_\mathrm{p}};$$

$$\rho = \frac{p\mu}{k_\mathrm{B} T_\mathrm{eq}}; \quad \beta_\mathrm{p} \equiv \frac{GM_\mathrm{p}\mu}{r_\mathrm{p} k_\mathrm{B} T_\mathrm{eq}}, \tag{1}$$

where the subscripts "p" and "∞" denote the quantities at the planetary radius and infinite radius, respectively, G is the gravitational constant, k_B is the Boltzmann constant, M_p is the planetary mass (core and atmosphere combined), μ is the (dimensional) mean molecular mass, and $T_\mathrm{eq} \simeq 886\,\mathrm{K}(L_*/L_\odot)^{1/4}(a/0.1\,\mathrm{au})^{-1/2}$ is the equilibrium temperature at planetary orbit radius a and host star luminosity L_*. The

dimensionless parameter β_p is also called the "restricted Jeans parameter" (e.g., Cubillos et al. 2017; Fossati et al. 2017). We also remind the reader that p_∞ in Equation (1) serves as a confining term preventing the isothermal atmosphere from a spontaneous outflow. If one naively assumes a clear atmosphere (free of cloud/haze) of solar abundance, $p_p \sim 20$–100 mbar is required at the observed transit radius (e.g., Lopez & Fortney 2014; Lammer et al. 2016). For Kepler 51b, this leads to $\beta_p \simeq 9.8$ and $p_\infty \sim 10^{-6}$ bar using Equation (1) Such p_∞ is a few orders of magnitude greater than any plausible Sun-like stellar wind total pressure (Murray-Clay et al. 2009). Unconfined atmospheres hydrodynamically lose mass at $\dot{M} \sim \min\{\dot{M}_{Parker}, \dot{M}_{rad}\}$, where (e.g., Parker 1958)

$$\dot{M}_{Parker} \sim 4\pi r_s^2 c_s \rho_p \exp\left(\frac{3}{2} - \frac{2r_s}{r_p}\right),$$

$$\dot{M}_{rad} \sim \left(\frac{L_*}{4\pi a^2}\right)\pi r_p^2 \left(\frac{c_s^2}{2}\right)^{-1}. \quad (2)$$

Here $c_s = (k_B T_{eq}/\mu)^{1/2}$ is the isothermal sound speed and $r_s = GM_p/(2c_s^2)$ is the sonic radius. We find $\dot{M} \sim 10^{-3} M_\oplus$ yr^{-1} with $p_p \sim 10$ mbar for Kepler 51b, dispersing the atmosphere in $\lesssim 10^3$ yr—much shorter than the estimated age of the system (~ 0.3 Gyr), which in turn questions the earlier assumption of "clear" atmosphere.

2.2. Dust in the Atmospheres

Aerosols, which could consist of dust and liquid droplets, could dramatically increase the opacity of gas. The enhanced opacity lowers the required pressure at the apparent planet radius p_p by several orders of magnitude, giving rise to a much slower outflow. However, maintaining aerosol particles at a radius as high as $7 R_\oplus$ over Kepler 51b is difficult in a static atmosphere. In-situ formation of dust (for clouds/haze) demands a rather high gas density; photochemical calculations reveal that dust formation is very inefficient below $p \sim 10^{-7}$–10^{-6} bar (Morley et al. 2012, 2013; Fortney et al. 2013; Kawashima & Ikoma 2018). Aerosols are also subject to planetary gravity; dust grains with radius r_d precipitate at terminal velocity v_{term} and timescale τ_{prec} (Baines et al. 1965; Draine 2011)

$$v_{term} \sim 3 \text{ m s}^{-1} \times \left(\frac{\mu}{m_H}\right)^{-1/2}\left(\frac{M_p}{M_\oplus}\right)\left(\frac{r}{R_\oplus}\right)^{-2}$$

$$\times \left(\frac{r_d}{10 \text{ Å}}\right)\left(\frac{\rho/m_H}{10^{12} \text{ cm}^{-3}}\right)\left(\frac{T}{10^3 \text{ K}}\right)^{-1/2};$$

$$\tau_{prec,p} \equiv \frac{r_p}{v_{term,p}} \sim 10^{-1} \text{ yr}\left(\frac{r_d}{10 \text{ Å}}\right)^{-1}\left(\frac{\rho_p/m_H}{10^{12} \text{ cm}^{-3}}\right). \quad (3)$$

The eddy diffusion coefficent required to lift $r_d = 10$ Å dust to $\sim 7 R_\oplus$ is at least $K_{zz} \sim 10^{11}$–10^{12} cm^2 s^{-1}, which is significantly greater than the values observed on Earth (Pilinski & Crowley 2015) and modeled on exoplanets (Morley et al. 2013). Even if dust formation at high altitudes were sufficient to compensate dust precipitation, in a static atmosphere with the Equation (1) density profile, heavy elements in this layer are rapidly depleted at timescale $\lesssim (m_{metal}/m_d)\tau_{prec}$ (here

(m_{metal}/m_d) is the atmospheric mass ratio of metal elements to dust).

We thus consider non-static atmospheres in which aerosols are co-moving with outflows. The critical mass-loss rate, at which $v_r = v_{term}$ (note that this equation does *not* depend on r; see also WD18)

$$\dot{M}_{crit} \equiv 4\pi r^2 \rho v_{term} \simeq 2 \times 10^{-11} M_\oplus \text{ yr}^{-1}\left(\frac{M_c}{M_\oplus}\right)$$

$$\times \left(\frac{r_d}{10 \text{ Å}}\right)\left(\frac{T}{10^3 \text{ K}}\right)^{-1/2}\left(\frac{\mu}{m_H}\right)^{1/2}. \quad (4)$$

Whenever $\dot{M} \gg \dot{M}_{crit}$, dust experiences negligible precipitation, and can be considered as co-moving with gas. $\dot{M}$ must also satisfy $\dot{M} < \dot{M}_{max} \sim (M_{atm}/\tau_p)$, where M_{atm} is the total mass of atmosphere and τ_p is the planet's age (approximated by the host star's age τ_*; for Kepler 51b, $\dot{M}_{max} \sim 10^{-9} M_\oplus$ yr^{-1}). Dust of ~ 10 Å sizes should be abundantly produced by geological activities, while laboratory experiments (Zhao et al. 2018) show that gas-phase formation of tiny graphites and polycyclic aromatic hydrocarbon (PAH) can also be very efficient even at relatively low temperatures and ultraviolet (UV) intensities. Meanwhile, the temperature throughout most of the internal atmosphere (Section 3.1) is higher than dust sublimation temperature (~ 1500 K), preventing tiny grains from coagulating quickly: larger grains fall back to the internal atmosphere and are broken into gaseous species.

2.3. Effective Transit Radii

High-altitude aerosols lead to extra extinction on stellar light from the observer's view, thus effectively increasing the planet trasiting radii. To ease later discussion, we define the effective transit radius:

$$\langle r_{eff} \rangle \simeq \left\{\frac{1}{\pi}\int_0^{R_H} db \; 2\pi b[1 - e^{-\tau(b)}]\right\}^{1/2}, \quad (5)$$

where $\tau(b)$ is the optical depth along the line of sight (LOS) at impact parameter b relative to the planet geometric center. The upper limit of the integral is R_H (the planet's Hill radius) where the assumption of excluding host star gravitation likely breaks down. We estimate the optical depth by $\tau(b) \simeq \Sigma(b)X_d\sigma_{d,ext}$, where $\Sigma(b)$ is the column density along the LOS, $X_d \simeq n_d/(\rho/m_H)$ is the number fraction of dust particles relative to hydrogen nuclei, and $\sigma_{d,ext}$ is the extinction cross section of a single dust particle. At optical and infrared (IR) wavelengths $0.2 \lesssim (\lambda/\mu\text{m}) \lesssim 2$, the extinction cross section of very small grains is well approximately given by a smooth power-law function,

$$\sigma_{d,ext} \simeq \sigma_{-16} \times 10^{-16} \text{ cm}^2\left(\frac{r_d}{10 \text{ Å}}\right)^3\left(\frac{\lambda}{\mu\text{m}}\right)^{-\delta}, \quad (6)$$

where $(\sigma_{-16}, \delta) \simeq (0.92, 1.55)$ for graphites, and $(0.11, 0.93)$ for silicates (Draine & Malhotra 1993). PAH grains at $r_d \sim 10$ Å have an absorption edge at $\lambda \sim 1 \mu$m, and are optically similar to graphites at shorter wavelengths (Li & Draine 2001). For simplicity we assume that all aerosols consist of graphite dusts. The dust-to-gas mass ratio

corresponding to number ratio X_d is, assuming hydrogen atmosphere,

$$\frac{m_d}{m_{gas}} \simeq X_d \left(\frac{m_C N_{C,dust}}{m_H} \right) \simeq 0.56 \left(\frac{r_d}{10 \text{ Å}} \right)^3 \left(\frac{X_d}{10^{-4}} \right), \qquad (7)$$

where $N_{C,dust} \simeq 470 \, (r_d/10 \text{ Å})^3$ is the number of carbon atoms per dust grain.

3. Detailed Modeling

3.1. Isentropic Interior

Although all interesting atmospheric dynamics take place in the radiative exterior, hydrodynamic structures of the convective interior should still be consistently calculated by solving

$$\frac{dM_a}{dr} = 4\pi r^2 \rho, \quad \frac{dp}{dr} = -\frac{G(M_a + M_c)\rho}{r^2}, \quad p = \kappa \rho^\gamma, \qquad (8)$$

where M_a is the mass of atmosphere enclosed by radius r, M_c is the mass of the solid planet core, κ is the specific entropy parameter, and γ is the adiabatic index (we take $\gamma = 1.4$ for the molecular atmospheres in this Letter).

The gravitation in the radiative exterior of atmosphere depends on both M_c and the total mass of isentropic atmosphere M_{atm}, while the self-gravity of the gas in that layer is usually negligible. In practice, we first pick an M_c and an M_{atm} and obtain a model of the external radiative atmosphere. Then, we solve Equation (8) as a boundary value problem such that (1) $M_a(R_c) = 0$ (R_c is the planet core radius), and (2) p and ρ match the external atmosphere profiles at the radiative-convective boundary r_{rcb}, which is adjusted so that $M_a(r_{rcb}) = M_{atm}$. The isentropic atmosphere is characterized by its Kelvin–Helmholtz timescale τ_{kh} (e.g., Owen & Wu 2017).

3.2. Dusty Outflowing Exterior

The model planet orbits the host star (for simplicity, we round off to $M_* = M_\odot$, $L_* = 0.88 L_\odot$ from M14) on a $a = 0.25$ au circular orbit ($T_{eq} = 543$ K). The planet combines an $M_c = 1.7 \, M_\oplus$, $R_c = 1.14 \, R_\oplus$ solid core and an $M_{atm} = 0.4 \, M_\oplus$ convective atmosphere.

3.2.1. Model 0: Isothermal Parker Wind

The first model (Model 0) that we consider is constructed *analytically*. If we assume an isothermal $T = T_{eq}$, the well-known Parker wind solution satisfies (Parker 1958),

$$\exp\left(-\frac{\mathcal{M}^2}{2} \right) = \varrho \exp\left(\frac{3}{2} - \frac{2}{\eta} \right), \quad \varrho = \frac{1}{\mathcal{M}\eta^2}, \qquad (9)$$

where $\mathcal{M} \equiv v_r/c_s$ is the radial Mach number, $\eta \equiv r/r_s$ is the dimensionless radius normalized by the sonic radius r_s, and $\varrho \equiv \rho/\rho_s$ is the dimensionless density normalized by ρ_s (the density at sonic radius).

3.2.2. Consistent Thermochemical Simulations

Models 1 and 2 involve full hydrodynamic simulations that incorporate radiation and thermochemistry described in WD18. The axisymmetric 2.5-dimensional spherical-polar mesh centers at the planet, whose polar axis points to the host star. It spans $(r, \theta) \in [3 \, R_\oplus, 400 \, R_\oplus] \otimes [0, \pi]$ at resolution $256 \times$

Table 1
Properties of the Representative Models

Model	τ_{kh} (10^9 yr)	$\rho_{ini}(r_{in})$ (10^{-8} g cm^{-3})	m_d/m_{gas} (10^{-2})	$\dot{M}_{-10}$[a]
0 (Parker wind)	2.3	18.9	1.7	4.0
1 (Optical and IR)	6.2	0.37	2.6	5.4
2 (UV and X-ray)			4.8	6.5

Note. All models have $\langle r_{eff} \rangle = 7 \, R_\oplus$ at $\lambda = 1 \, \mu$m.
[a] $\dot{M} \equiv \dot{M}_{-10} \times 10^{-10} \, M_\oplus$ yr^{-1}.

128 (radial zones are spaced logarithmically and latitudinal zones evenly), to guarantee that all relevant physical processes are included in the simulation domain. The initial conditions obey the isothermal hydrostatics at T_{eq} in Equation (1), where $\rho_{ini}(r_{in})$ (the initial mass density at the inner boundary $r_{in} = 3 \, R_\oplus$) is the variable parameter. Initial abundances of chemical species are uniform across the simulation domain; they are identical to WD18, except for the dusts. We adjust $\rho_{ini}(r_{in})$ and the dust-to-gas mass ratio (m_d/m_{gas}) for each simulation so that $\langle r_{eff} \rangle = r_p = 7 \, R_\oplus$ and $\dot{M}_{max} > \dot{M} \gg \dot{M}_{crit}$ in steady states.

Both models include the host star luminosity $L(2 \text{ eV}) = 0.88 \, L_\odot$, representing infrared (IR) and optical radiation. Model 2 also involves high-energy photons represented by four photon energy bins ($h\nu = 7$ eV for soft far-UV (FUV), 12 eV for Lyman–Werner band FUV, 25 eV for extreme-ultraviolet (EUV), and 3 keV for the X-ray) at luminosities[4]: $L(7 \text{ eV}) = L(25 \text{ eV}) = L(3 \text{ keV}) = 8 \times 10^{28}$ erg s^{-1}, and $L(12 \text{ eV}) = 8 \times 10^{27}$ erg s^{-1}. Rays are parallel to the polar axis, entering the simulation domain at the outer radial boundary with fluxes $F(h\nu) = L(h\nu)/(4\pi a^2)$.

We include $r_d = 10$ Å graphites in these two models as a proxy of dusts of all sizes and components. Dust temperature is estimated by the dual-temperature profile $T_d = \max\{T_{eq}, \tilde{T}_d\}$ (similar to Chiang & Goldreich 1997), where $\tilde{T}_d$ is obtained by solving

$$\sum_{h\nu} F(h\nu) \sigma_{d,ext}(h\nu) = 4\pi r_d^2 \sigma_{SB} \tilde{T}_d^4 q(\tilde{T}_d). \qquad (10)$$

Here σ_{SB} is the Stefan–Boltzmann constant, and $q(T_d)$ is the dust emissivity.

3.3. Results

3.3.1. Model Profiles

Table 1 summarizes the key properties and results of our models. All models demand $\sim 10^{-2}$ of atmospheric mass in dusts to achieve $\langle r_{eff} \rangle = 7 \, R_\oplus$ with $M_p = 2.1 \, M_\oplus$. The gas pressure required at r_p is merely $\sim 10^{-8} - 10^{-9}$ bar, while the $p = 100$ mbar radii is much lower (compared to Section 2.1): $r_{100 \text{ mbar}} \simeq 2.5 \, R_\oplus$ (Model 0) or $2.2 \, R_\oplus$ (Models 1 and 2). Density, temperature and radial velocity profiles along the radial ray at $\theta = \pi/2$ (i.e., perpendicular to the direction to the host star) of all models are presented by Figure 1. Figure 2 illustrates the meridional plots of density, temperature, and velocity profiels for Model 2 in steady state, which are similar

---

[4] These high-energy luminosities are estimated with the recipes in Owen & Wu (2017) and WD18, adopting Ribas et al. (2005) for $L(t < 10^8 \text{ yr})$ and assuming $L/L(t < 10^8 \text{ yr}) = \min\{1, (\tau_*/10^8 \text{ yr})^{-1.5}\}$.
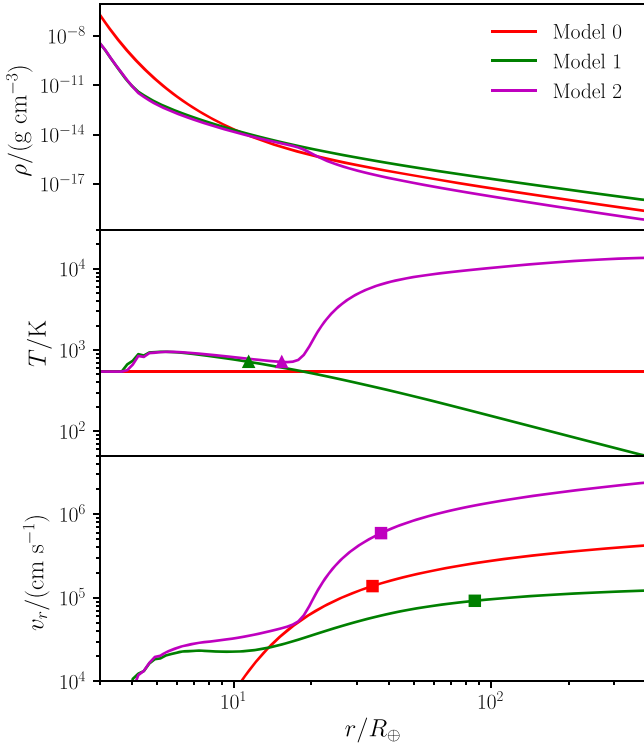
Figure 1. Hydrodynamic profiles (top: density ρ; middle: temperature T; bottom: radial velocity v_r) of models in Table 1 along the $\theta = \pi/2$ radii. Models are distinguished by colors. Triangles mark the locations wher gas thermally decouples from dusts (above which $|T_d - T|/T_d > 0.3$) for Models 1 and 2. Squares mark the radial sonic points ($v_r = c_s$).

to the EUV photoevaporation models discussed in WD18: a hot ($T > 10^4$ K), anisotropic EUV-dominated outflow, a warm ($T \lesssim 10^3$ K) intermediate layer, and a "tail" behind the night hemisphere.

Curiously, there are also day–night meridional motions in Models 1 and 2. This is the consequence of dust temperature excess: in regions accessible by $h\nu = 2$ eV photons, dust temperature $T_d \simeq 1050$ K $\gg T_{eq}$ due to $q(T_d) \ll 1$ (Equation (10)), causing gas temperature $T \gg T_{eq}$ via dust-gas thermal accommodation. Figure 2 illustrate such meridional motion, which never leaves the planetary gravity potential, but still satisfies $|v| \gg v_{term}$ hence can keep the dust aloft. We nonetheless choose not to over-interpret this result: atmospheric circulation requires proper treatment of radiative transfer, dimensionality, and planet spin to model, which are left for future works.

3.3.2. Transit Light Curves and Model Consistency

Figure 3 illustrates the synthetic transit light curves (limb-darkening profile adopted from M14), plus a simple "hard sphere" for reference. All models have a extended but gentler ingress/egress than the hard sphere. Model 2 has a relatively sharper ingress/egress, because EUV photons carve a cliff in density and temperature by launching a photoevaporative wind. The synthetic light curve is symmetric about the mid-transit, as $\langle r_{eff} \rangle = 7\, R_\oplus$ is still deep in the planet's potential well. To analyze the detectability of the difference in the light curves, we re-sample systhetic light curves with 1 minute cadence and add a white noise component of 1500 ppm to mimic the *Kepler* observation of Kepler 51b. The resultant light curves were
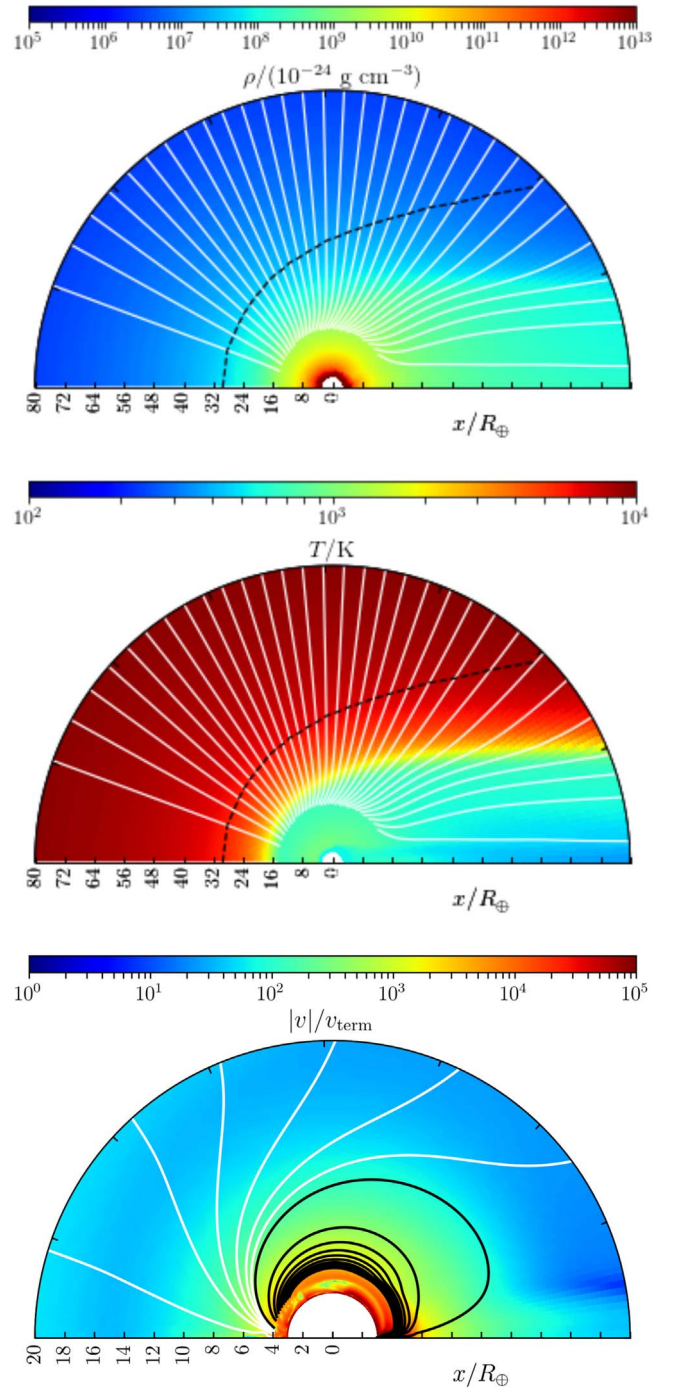

Figure 2. Meridional plot of Model 2 (Section 3.2.2) in steady state, showing density ρ (top panel), temperature T (lower panel), and $|v|/v_{term}$ (bottom panel, zoomed-in for the innermost $20\, R_\oplus$) profiles. The top and middle panels are overlaid by streamlines in white solid curves, separated by mass flow $2 \times 10^{-11}\, M_\oplus\, yr^{-1}$, shown only in regions where the total energy of fluid elements is positive. Sonic surface is overlaid with black dashed curves. The bottom panel zooms in for two types of streamlines: white curves are streamlines that eventually join the EUV wind and escape to infinity, separated by $10^{-10}\, M_\oplus\, yr^{-1}$ mass flow; black curves are streamlines that eventually fall back, separated by $10^{-9}\, M_\oplus\, yr^{-1}$ mass flow. Only the $r \geqslant 4\, R_\oplus$ part (approximately the radius of $h\nu = 2$ eV radiation front in the day hemisphere) of streamlines are presented.

analyzed with a conventional Mandel & Agol (2002) transit model similar to that employed by M14. We found that more extended and gentler ingress/egress of the synthetic light
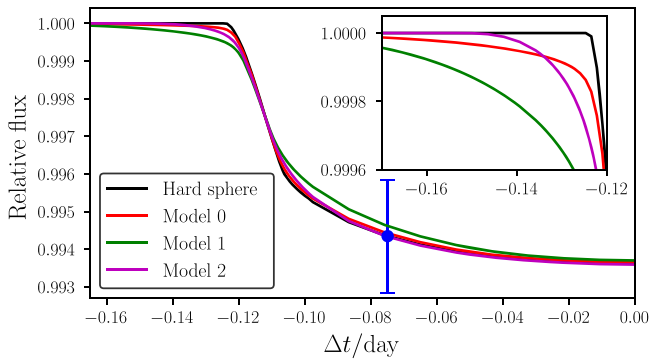
Figure 3. Transit light curves of our models (Models 0 through 2, plus a hard sphere for reference), showing only the range $\Delta t < 0$ ($\Delta t > 0$ curves are omitted due to symmetry). An errorbar is overlaid to indicate the typical error of Kepler short-cadence measurement. The inserted panel zooms in the light curves near the ingress. Our dusty outflow models all produce a gentler ingress/egress compared to the hard sphere model. However, after analyzing the Kepler light curve, we found that these models cannot be decidedly ruled out due to the large observation uncertainty.

curves can be accommodated by a combination of higher impact parameter b and slightly different limb-darkening coefficients than those reported by M14. A future observation of the system with higher photometric precision is required to distinguish Models 0 through 2, which differs by only $\sim$200 ppm.

4. Discussion and Summary

In this Letter, we showed that a dusty outflow of a planetary atmosphere could enhance the opacity at high altitudes, therefore it successfully explains the puffy Kepler 51b and the flat transmission spectrum of super-puff exoplanets. The dusty outflow scenario relies on the mass loss rate $\dot{M}$, which should stay in a proper range ($\dot{M}_{crit} \ll \dot{M} \ll \dot{M}_{max}$; see Section 2.2), favoring the class of young, low-mass sub-Neptunes. Cubillos et al. (2017) suggested that $\sim$15% of sub-Neptunes are too puffy and may be currently experiencing mass loss. The mechanism is maximized when the atmospheric dispersal timescale is similar to the age of the system (e.g., $\sim$0.3 Gyr for Kepler 51 (M14), and $\lesssim$1 Gyr for Kepler 79 Walkowicz & Basri 2013).

Dusty outflows have several implications. First, extinction cross sections of small grains are smooth function of wavelengths in optical and near-IR (see also Draine & Lee 1984; Draine & Malhotra 1993; Li & Draine 2001). Dust therefore obscures the signatures of some other chemical species in planetary atmospheres, limiting the ability of transmission spectroscopy. Figure 4 plots the strength of water features against planet mass for sub-Neptune planets (Crossfield & Kreidberg 2017). We note a possible dichotomy that only low-mass ($\lesssim$10 $M_{\oplus}$) planets tend to have muted absorption features. One explanation is that planets more massive than 10 M have gravitational wells that are too strong to allow adequate atmospheric loss, as seen in numerical explorations of WD18. Meanwhile, due to the large optical depths in Lyα (Draine 2011) and the metastable helium line (Oklopcic & Hirata 2018), a simple calculation shows that both lines should still be observable by transmission spectra for planets undergoing dust outflows. Second, the observed r_p may differ significantly from the predicted radius assuming a clear atmosphere (Section 3.3). A key objective of the Transiting Exoplanet Survey Satellite mission is to accurately measure the masses and radii of >50 sub-Neptunes, followed by ensemble analyses of their
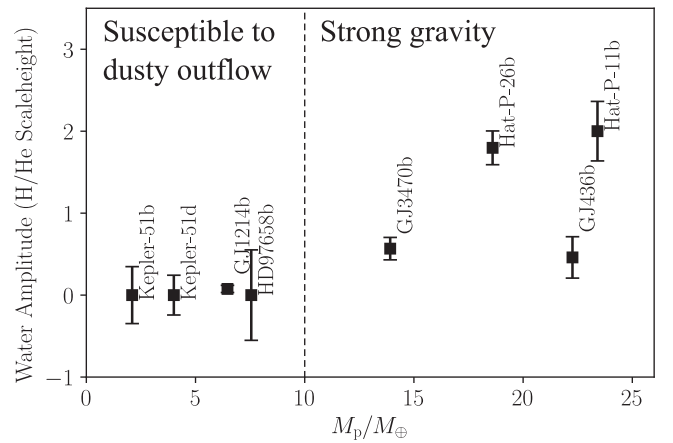

Figure 4. Spectral strenths of water feature vs. planet mass, compiled by Crossfield & Kreidberg (2017); data of Kepler 51b and 51d are from Roberts et al 2019, in preparation. According to our earlier simulations (WD18), below $\sim$10 $M_{\oplus}$ are the objects that are susceptible to dusty outflows, while $M_p > 10\,M_{\oplus}$ planets have gravity that is too strong to efficiently launch outflows.

compositions, which may be significantly biased if leaving dusty outflows unaccounted for. Third, as $\sigma_{d,ext}$ increases at shorter wavelengths, $\langle r_{eff} \rangle$ in optical bands should be greater than IR. The transiting radii yielded by Equation (6) at $\lambda = 0.5\,\mu$m are $\sim$10%–20% greater than $\lambda = 1\,\mu$m. Such a phenomenon has been observed for a few exoplanets (e.g., Ehrenreich et al. 2014). Extending wavelength coverage of transmission spectra (e.g., *Spitzer*) should also allow for the detection of more dust-specific signatures.

ORCID iDs

Lile Wang ⓘ https://orcid.org/0000-0002-6540-7042
Fei Dai ⓘ https://orcid.org/0000-0002-8958-0683

References

Baines, M. J., Williams, I. P., & Asebiomo, A. S. 1965, MNRAS, 130, 63
Chiang, E. I., & Goldreich, P. 1997, ApJ, 490, 368
Crossfield, I. J. M., & Kreidberg, L. 2017, AJ, 154, 261
Cubillos, P., Erkaev, N. V., Juvan, I., et al. 2017, MNRAS, 466, 1868
Draine, B. T. 2011, Physics of the Interstellar and Intergalactic Medium (Princeton, NJ: Princeton Univ. Press)
Draine, B. T., & Lee, H. M. 1984, ApJ, 285, 89
Draine, B. T., & Malhotra, S. 1993, ApJ, 414, 632
Ehrenreich, D., Bonfils, X., Lovis, C., et al. 2014, A&A, 570, A89
Fortney, J. J., Mordasini, C., Nettelmann, N., et al. 2013, ApJ, 775, 80
Fossati, L., Erkaev, N. V., Lammer, H., et al. 2017, A&A, 598, A90
Fulton, B. J., Petigura, E. A., Howard, A. W., et al. 2017, AJ, 154, 109
Ginzburg, S., Schlichting, H. E., & Sari, R. 2016, ApJ, 825, 29
Howe, A. R., & Burrows, A. 2015, ApJ, 808, 150
Jontof-Hutter, D., Lissauer, J. J., Rowe, J. F., & Fabrycky, D. C. 2014, ApJ, 785, 15
Kawashima, Y., & Ikoma, M. 2018, ApJ, 853, 7
Kreidberg, L., Bean, J. L., Désert, J.-M., et al. 2014, Natur, 505, 69
Lammer, H., Erkaev, N. V., Fossati, L., et al. 2016, MNRAS, 461, L62
Li, A., & Draine, B. T. 2001, ApJ, 554, 778
Lopez, E. D., & Fortney, J. J. 2014, ApJ, 792, 1
Lopez, E. D., Fortney, J. J., & Miller, N. 2012, ApJ, 761, 59

Mandel, K., & Agol, E. 2002, ApJL, 580, L171
Masuda, K. 2014, ApJ, 783, 53
Morley, C. V., Fortney, J. J., Kempton, E. M.-R., et al. 2013, ApJ, 775, 33
Morley, C. V., Fortney, J. J., Marley, M. S., et al. 2012, ApJ, 756, 172
Murray-Clay, R. A., Chiang, E. I., & Murray, N. 2009, ApJ, 693, 23
Ofir, A., Dreizler, S., Zechmeister, M., & Husser, T.-O. 2014, A&A, 561, A103
Oklopcic, A., & Hirata, C. M. 2018, ApJL, 855, L11
Owen, J. E., & Wu, Y. 2016, ApJ, 817, 107

Owen, J. E., & Wu, Y. 2017, ApJ, 847, 29
Parker, E. N. 1958, ApJ, 128, 664
Pilinski, M. D., & Crowley, G. 2015, JGRA, 120, 3097
Rafikov, R. R. 2006, ApJ, 648, 666
Ribas, I., Guinan, E. F., Güdel, M., & Audard, M. 2005, ApJ, 622, 680
Walkowicz, L. M., & Basri, G. S. 2013, MNRAS, 436, 1883
Wang, L., & Dai, F. 2018, ApJ, 860, 175
Zhao, L., Kaiser, R. I., Xu, B., et al. 2018, NatAs, 2, 973